MIT Open Access Articles

HOT GASEOUS CORONAE AROUND SPIRAL GALAXIES: PROBING THE ILLUSTRIS SIMULATION

HOT GASEOUS CORONAE AROUND SPIRAL GALAXIES: PROBING THE ILLUSTRIS SIMULATION

Ákos Bogdán[1], Mark Vogelsberger[2], Ralph P. Kraft[1], Lars Hernquist[1], Marat Gilfanov[3,4], Paul Torrey[2,5],
Eugene Churazov[3,4], Shy Genel[1], William R. Forman[1], Stephen S. Murray[1,6], Alexey Vikhlinin[1],
Christine Jones[1], and Hans Böhringer[7]
[1] Harvard-Smithsonian Center for Astrophysics, 60 Garden Street, Cambridge, MA 02138, USA; abogdan@cfa.harvard.edu
[2] Department of Physics, Kavli Institute for Astrophysics and Space Research, Massachusetts Institute of Technology, Cambridge, MA 02139, USA
[3] Max-Planck-Institut für Astrophysik, Karl-Schwarzschild-strasse 1, D-85748 Garching, Germany
[4] Space Research Institute, Russian Academy of Sciences, Profsoyuznaya 84/32, 117997 Moscow, Russia
[5] TAPIR, Mailcode 350-17, California Institute of Technology, Pasadena, CA 91125, USA
[6] Department of Physics and Astronomy, Johns Hopkins University, 3400 North Charles Street, Baltimore, MD 21218, USA
[7] Max Planck Institute for extraterrestrial Physics, Giessenbachstrae 1, D-85748 Garching, Germany

ABSTRACT

The presence of hot gaseous coronae around present-day massive spiral galaxies is a fundamental prediction of galaxy formation models. However, our observational knowledge remains scarce, since to date only four gaseous coronae have been detected around spirals with massive stellar bodies ($\gtrsim 2 \times 10^{11}\, M_\odot$). To explore the hot coronae around lower mass spiral galaxies, we utilized *Chandra* X-ray observations of a sample of eight normal spiral galaxies with stellar masses of $(0.7 - 2.0) \times 10^{11}\, M_\odot$. Although statistically significant diffuse X-ray emission is not detected beyond the optical radii ($\sim 20\,\mathrm{kpc}$) of the galaxies, we derive 3σ limits on the characteristics of the coronae. These limits, complemented with previous detections of NGC 1961 and NGC 6753, are used to probe the Illustris Simulation. The observed 3σ upper limits on the X-ray luminosities and gas masses exceed or are at the upper end of the model predictions. For NGC 1961 and NGC 6753 the observed gas temperatures, metal abundances, and electron density profiles broadly agree with those predicted by Illustris. These results hint that the physics modules of Illustris are broadly consistent with the observed properties of hot coronae around spiral galaxies. However, one shortcoming of Illustris is that massive black holes, mostly residing in giant ellipticals, give rise to powerful radio-mode active galactic nucleus feedback, which results in under-luminous coronae for ellipticals.

Key words: cosmology: theory – galaxies: ISM – galaxies: spiral – X-rays: galaxies – X-rays: general – X-rays: ISM

1. INTRODUCTION

The existence of gaseous X-ray coronae in the dark matter halos of massive galaxies is predicted by galaxy formation models (e.g., White & Rees 1978; White & Frenk 1991; Toft et al. 2002; Rasmussen et al. 2009; Crain et al. 2010; Vogelsberger et al. 2013; Marinacci et al. 2014). Although simulations agree that these hot coronae should be ubiquitous, various models make very different predictions. These disagreements originate from two sources. First, the incomplete realization of the physical processes may result in different galaxy populations. Specifically, many earlier models lacked efficient supernova and/or active galactic nucleus (AGN) feedback, which often yielded overly massive stellar components relative to their dark matter halos due to the strong gas cooling. Second, using different hydrodynamical schemes resulted in large systematic differences in the global state of baryons (Vogelsberger et al. 2012). Thus, the predicted properties of hot coronae also sensitively depend on the applied hydrodynamical scheme (Bogdán et al. 2013a). The ever-increasing computing power plays a major role in overcoming the issues related to incomplete modeling of the physical processes. Indeed, state-of-the-art simulations are now capable of studying large cosmological volumes combined with high numerical resolution, which simultaneously allows the study of large galaxy samples and robust modeling of complex physical processes (e.g., Vogelsberger et al. 2014a). Additionally, detailed tests help to understand the differences between

the recently developed moving mesh and the traditionally used smoothed particle hydrodynamics codes.

Although hot X-ray coronae are of fundamental importance, their detection and characterization pose major observational challenges around spiral galaxies, which offer a clean test of galaxy formation models (Bogdán et al. 2013a). The main difficulty is due to the faint but extended nature of the coronae around spirals, which in turn result in low signal-to-noise ratios (S/N). Additionally, the brightest X-ray coronae are associated with the most massive galaxies, which systems are rare in the local universe ($D \lesssim 100\,\mathrm{Mpc}$). Despite these challenges, numerous observational studies aimed to explore hot gaseous coronae around nearby spiral galaxies, which systems offer a clean test of galaxy formation models (e.g., Benson et al. 2000; Rasmussen et al. 2009). The first X-ray coronae around spirals have only recently been detected; *Chandra*, *XMM-Newton*, and *ROSAT* data revealed gaseous coronae around NGC 1961, UGC 12591, NGC 6753, and NGC 266 (Anderson & Bregman 2011; Dai et al. 2012; Bogdán et al. 2013a, 2013b). Due to the large distances of these galaxies and/or the relatively shallow X-ray observations, however, a detailed characterization of the coronae was only possible for NGC 1961 and NGC 6753 (Anderson & Bregman 2011; Bogdán et al. 2013a).

Despite these advances, the presently available sample is scarce and only includes massive galaxies ($M_\star \gtrsim 2 \times 10^{11}\, M_\odot$), which presents limitations for using the hot coronae as probes of galaxy formation models. While extraplanar diffuse emission has been detected around several lower mass

spiral galaxies (Li et al. 2006, 2011; Bogdán & Gilfanov 2008), this gaseous emission cannot be attributed to the hot corona of infalling gas. Indeed, the diffuse gas in these galaxies does not extend to large radii. It also exhibits a bipolar morphology, which when combined with the mass and energy budget of the galaxies, hint that the gas is outflowing and the outflows are sustained by the energy input from type Ia supernovae. Additionally, several studies have explored the presence of diffuse emission within the central regions of spiral galaxies (Li & Wang 2013; Li et al. 2014). Although a certain fraction of this emission may originate from the infalling hot gas, it is nearly impossible to disentangle this emission from other diffuse X-ray emitting components, in particular from the hot gas associated with star formation. Therefore, it is desirable to probe hot coronae *beyond* the optical radii of the galaxies. Exploring extended X-ray coronae around lower mass spirals will allow us to place stronger constraints on galaxy formation simulations and to probe a broader galaxy population. However, due to their faint nature, the X-ray coronae may remain undetected around galaxies with $M_\star < 2 \times 10^{11}\, M_\odot$. While non-detections only allow limits on various properties of the coronae, these limits provide invaluable input to probe galaxy formation models. Thus, the goal of this work is to extend the current sample with a focus on lower mass spiral galaxies.

The Illustris Simulation, which is based on the moving-mesh code AREPO (Springel 2010), offers an ideal framework to compare the observational results with those predicted by a modern hydrodynamical cosmological simulation. Illustris includes the main physical processes that influence galaxy evolution, such as primordial and metal line cooling, star formation, chemical enrichment, energetic feedback from supernovae, and AGN (Vogelsberger et al. 2014b). Therefore, Illustris provides a realistic galaxy population of elliptical and spiral galaxies (Vogelsberger et al. 2013). Additionally, because Illustris was performed in a large cosmological box, which consists of a broad population of spiral galaxies with $M_\star \gtrsim 10^{11}\, M_\odot$, this allows a comparison with observational results. Thus, the goal of our study is to probe hot X-ray coronae around spiral galaxies and compare the observed properties with those predicted by Illustris.

The paper is structured as follows. In Section 2 we introduce the observed and simulated galaxy sample. In Section 3 the data reduction is described. We present the results in Section 4, where we discuss the constraints on the characteristics of the hot X-ray coronae. In Section 5 we compare the observed and predicted properties of the coronae. We discuss our results in Section 6 and summarize in Section 7.

2. GALAXY SAMPLES

2.1. The Observed Galaxy Sample

To probe the hot X-ray coronae around spiral galaxies, we utilize *Chandra* X-ray observations. While *XMM-Newton* offers larger effective area, a particular advantage of *Chandra* is its lower and more stable instrumental background level, which makes it ideal to study the faint X-ray emission expected from hot coronae around spiral galaxies with $M_\star < 2 \times 10^{11}\, M_\odot$.

To this end, we searched for spiral galaxies with publicly available *Chandra* observations. To ascertain the morphological type of the galaxies, we relied on the HyperLeda database

and included Sa–Sc systems. We further filtered the sample by selecting galaxies in the distance range of $14 < D < 40$ Mpc. The lower distance boundary ensures that at least the inner regions of the coronae can fit in the *Chandra* field of view, while the higher boundary was introduced to maximize the S/N. We also required the sample galaxies to be sufficiently massive ($M_\star > 7 \times 10^{10}\, M_\odot$), which ensures that they reside in a massive dark matter halo, and host a more luminous and hotter X-ray corona. Additionally, we excluded galaxies that were located in rich galaxy groups/clusters, and only retained field galaxies or systems residing in poor groups with <20 members. This ensures that we probe the hot corona associated with the galaxy and not a larger-scale group/cluster atmosphere. Moreover, we excluded galaxies undergoing a significant merger event because the dark matter halos, and hence the hot gaseous coronae, of these galaxies may be disturbed. Finally, we removed starburst galaxies (for details see Section 6) and systems with high star-formation rates (SFRs) ($>10\, M_\odot\, yr^{-1}$), because they could be prone to starburst-driven winds. Based on these criteria, we identified six nearby spiral galaxies.

This sample was further expanded by two additional spiral galaxies, NGC 266 and ESO 445-081. While these galaxies are more distant, their *ROSAT* observations indicate the presence of luminous X-ray coronae (Bogdán et al. 2013b). Thus, we used follow-up *Chandra* observations to further study these galaxies.

Figure 1 shows the DSS B-band images of the eight spiral galaxies in our sample. While all galaxies reveal late-type morphologies, they exhibit a wide range of inclinations from face-on to edge-on systems. The physical properties of these spirals are listed in Table 1.

2.2. The Simulated Galaxy Sample

To compare the observed characteristics of the coronae with those predicted by Illustris, we used two approaches. First, we selected all galaxies, independent of their morphological types, whose stellar mass was in the range of $(0.2 - 20) \times 10^{11}\, M_\odot$. Due to their shallow potential well, the dominant fraction of galaxies with $M_\star < 2 \times 10^{10}\, M_\odot$ cannot confine a significant amount of hot X-ray gas. This approach offers a statistically significant galaxy sample, allowing us to characterize the gaseous coronae from low stellar mass systems to the most massive galaxies. Additionally, this large galaxy sample removes the distorting effects of outliers, which ensures that we can explore the general trends in the simulated properties of the hot coronae.

Second, we analyzed a sub-sample of spiral galaxies that were selected by Vogelsberger et al. (2014a). These 42 "textbook" spirals are sufficiently massive, disk-dominated systems. These spirals are the analogs of the observed galaxy sample, and thus offer an ideal basis to confront the *Chandra* observations with the Illustris Simulation.

3. DATA REDUCTION

3.1. Chandra X-ray Observations

The analysis of the *Chandra* data was performed with standard CIAO tools (version 4.6 and CALDB version 4.6.2). For each galaxy we analyzed all available ACIS-S or ACIS-I observations. The total combined exposure time of the
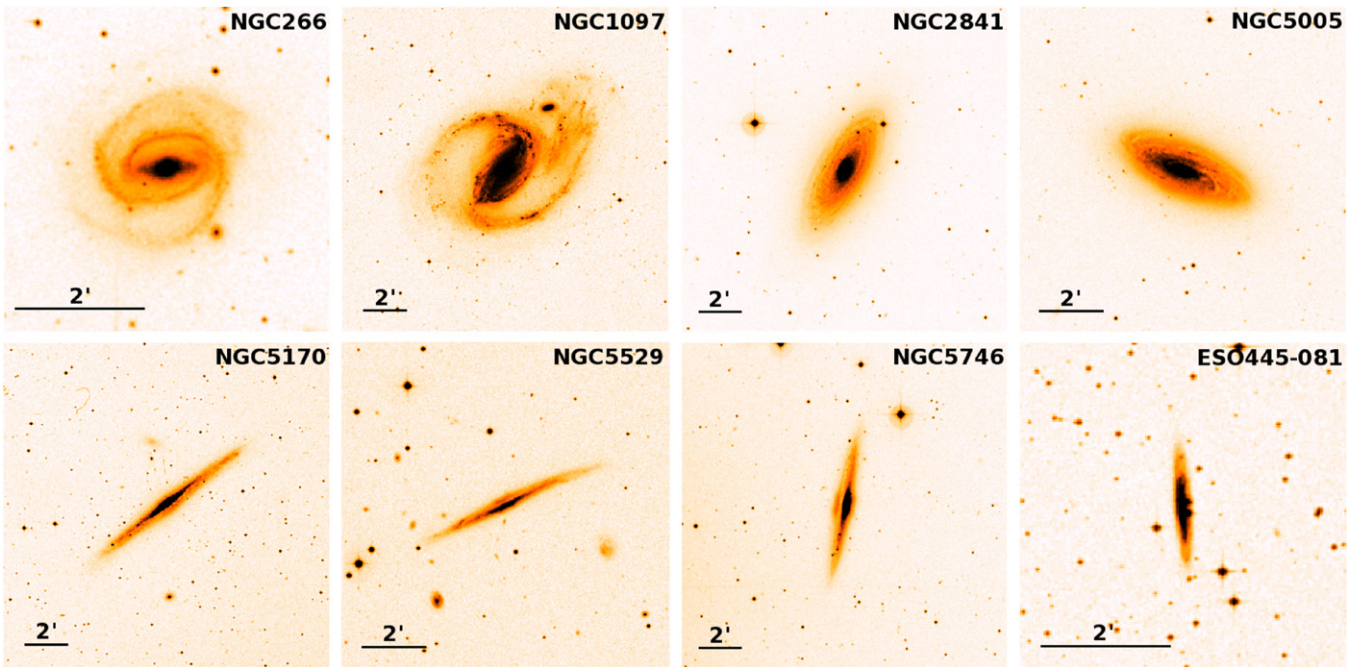
Figure 1. DSS B-band images of the spiral galaxies in our sample. All galaxies reveal late-type morphologies and have a prominent disk component. The images show that the selected galaxies are relatively undisturbed, only NGC 1097 may be experiencing a minor merger. The sample galaxies exhibit a wide range of inclinations, including face-on and edge-on systems.

Table 1
The Properties of the Sample Galaxies

| Name | Distance | $1'$ scale | N_H | L_K | $M_\star/L_K$ | $M_\star$ | SFR | Morph. | r_{200} | D_{25} |
| | (Mpc) | (kpc) | (cm^{-2}) | ($L_{K,\odot}$) | ($M_\odot/L_{K,\odot}$) | ($M_\odot$) | ($M_\odot$ yr^{-1}) | type | (kpc) | ($'$) |
	(1)	(2)	(3)	(4)	(5)	(6)	(7)	(8)	(9)	(10)
NGC 266	60.3	17.55	5.7×10^{20}	2.5×10^{11}	0.80	2.0×10^{11}	2.4	Sab	410	2.95
NGC 1097	14.2	4.12	2.0×10^{20}	1.3×10^{11}	0.77	1.0×10^{11}	5.8	SBb	238	10.47
NGC 2841	14.1	4.09	1.3×10^{20}	1.5×10^{11}	0.78	1.2×10^{11}	0.8	Sb	363	6.92
NGC 5005	18.5	5.38	1.1×10^{20}	1.9×10^{11}	0.77	1.4×10^{11}	4.9	SABb	273	4.79
NGC 5170	21.6	6.29	6.7×10^{20}	8.5×10^{10}	0.83	7.1×10^{10}	0.4	Sc	269	7.94
NGC 5529	36.0	10.45	1.0×10^{20}	1.0×10^{11}	0.75	7.8×10^{10}	2.0	Sc	314	5.75
NGC 5746	19.8	5.79	3.4×10^{20}	1.4×10^{11}	0.77	1.1×10^{11}	0.6	SABb	353	7.24
ESO 445-081	69.3	20.16	5.0×10^{20}	1.2×10^{11}	0.78	9.4×10^{10}	5.6	SBbc	590	1.70

Note. Columns are as follows. (1) Distance taken from Tully et al. (2009) (2) $1'$ scale at the adopted distance. (3) Line-of-sight column density provided by the LAB survey (Kalberla et al. 2005). (4) Total K-band luminosity from 2MASS. (5) K-band mass-to-light ratios computed from Bell et al. (2003) using the $B - V$ color indices of galaxies. (6) Total stellar mass based on the K-band luminosity and the K-band mass-to-light ratios. (7) Star-formation rate computed from the *IRAS* 60 μm and 100 μm flux—for details see Section 3.2. (8) Morphological type, taken from HyperLeda. (9) Virial radius of the galaxies, estimated from the maximum rotation velocity following Bogdán et al. (2013a). (10) Major axis diameter of the D_{25} ellipse.

analyzed data is 648.5 ks. The analyzed *Chandra* observations are listed in Table 2.

The first step of the data analysis was to reprocess all observations using the CHANDRA_REPRO task, which resulted in enhanced data quality and better calibrated observations. Then we identified and removed time intervals that were contaminated with background flares. Since the detectors are most sensitive to flares in the 2.3–7.3 keV band, we used this energy range to identify high background periods. For each observation, we excluded those time intervals that were 2σ above the mean count rate level. Removing the flares results in a $\approx$12% drop in the exposure times, and a total net exposure time of 574.2 ks. However, note that the ACIS-S detectors are more susceptible to background flares, so a larger fraction of contaminated time intervals were excluded from these data (Table 2).

In general, bright point sources can add a significant contribution to the truly diffuse gaseous emission, hence it is necessary to exclude them when studying diffuse X-ray emitting components. To detect bright point sources, we ran the WAVDETECT task using the parameters described in Bogdán & Gilfanov (2008). This procedure results in sufficiently large source cells that include $\gtrsim$97% of the source counts. These source cells were used to mask out bright point sources from further study of the diffuse emission.

To account for vignetting effects and convert the observed counts-to-flux units, we produced exposure maps assuming a thermal plasma model (APEC in XSPEC). The temperature of the model was 0.2 keV and the metal abundances were set to 0.1 Solar (Grevesse & Sauval 1998). The particular choice of spectrum was motivated by the results of our earlier observations (Bogdán et al. 2013a) and the Illustris simulation.

Table 2
The List of Analyzed *Chandra* Observations

Galaxy	Obs ID	T_{obs} (ks)	T_{filt} (ks)	Instrument
NGC 266	16013[a]	85.0	85.0	ACIS-I
NGC 266	16301	41.5	41.5	ACIS-I
NGC 1097	1611[a]	5.4	5.0	ACIS-S
NGC 1097	2339	5.7	5.0	ACIS-S
NGC 2841	389	1.8	1.8	ACIS-S
NGC 2841	6096[a]	28.2	21.3	ACIS-S
NGC 5005	4021	4.9	4.7	ACIS-S
NGC 5170	3928	33.0	33.0	ACIS-I
NGC 5529	4163	89.2	71.0	ACIS-I
NGC 5529	12255	60.4	50.8	ACIS-S
NGC 5529	12256[a]	118.5	96.0	ACIS-S
NGC 5529	13118	44.6	38.3	ACIS-S
NGC 5529	13119	54.3	48.0	ACIS-S
NGC 5746	4021	36.8	33.6	ACIS-I
ESO 445-081	16302	39.2	39.2	ACIS-I

[a] The coordinate system of these observations was used as reference when merging observations.

Indeed, Illustris predicts similar gas temperatures for a hot corona surrounding a galaxy with $M_\star = 10^{11} M_\odot$, which is close to the median stellar mass of our sample. Additionally, we observed sub-solar metal abundances ($\sim$0.1 Solar) for NGC 1961 and NGC 6753, which is in fair agreement with that predicted by Illustris (Section 5.3).

Since we aimed to study the faint diffuse X-ray emission, it is crucial to precisely account for the background emission. We used two different approaches to subtract the background components. For the more distant galaxies in our sample, we used local fields to subtract the background level. Using internal background fields offers a robust way to subtract all background components without the need to renormalize the background level. We note that due to the large virial radii of the galaxies in our sample, the applied background regions may be within the extended coronae of the galaxies. However, at large radii ($\gtrsim 0.3 r_{200}$) the gas is expected to have very low density (see Figure 6), implying that the extended coronae remain well below the detection threshold. To confirm this we extracted surface brightness profiles of the sample galaxies in the 0.3–2 keV energy range, and found that the vignetting corrected profiles do not show variations at these large radii. This hints that at radii $\gtrsim 0.3 r_{200}$ the contribution of gaseous coronae are negligible compared to the sky and instrumental background components. For the more nearby galaxies in our sample, we relied on the ACIS blank-sky background files to subtract the background components. To make sure that the soft X-ray sky background of the sample galaxies was similar to that of the background maps, we checked the fluxes of *ROSAT* All-sky Survey R4-R5 band images at the position of the galaxies (Snowden et al. 1997). We found that the galaxies in our sample had similar soft X-ray brightness to those used for constructing the ACIS background files. Due to the stable spectrum of the instrumental background, the *Chandra* blank-sky files can be tailored to a specific observation. To this end, we normalized the blank-sky background files using the observed count rate ratios in the 10–12 keV band. The accuracy of these background subtraction methods was compared for those galaxies, where both procedures could be applied. We concluded that the background subtracted data in these galaxies were in good agreement with each other, and the accuracy of background subtraction is a few percent.

3.2. Near- and Far-infrared Data

The near-infrared images offer a robust means to trace the stellar light. Therefore, we relied on the K-band images of the 2MASS to derive the stellar mass of the galaxies (Jarrett et al. 2003). Using the K-band magnitudes and the distances of the galaxies we derived the absolute K-band magnitudes and luminosities following the procedure described in Bogdán et al. (2013a). The K-band luminosities were converted to stellar mass using the mass-to-light ratios computed from the corresponding $B - V$ color indices and results of galaxy evolution modeling (Bell et al. 2003).

The SFRs of the sample galaxies are computed from the 60 and 100 μm far-infrared fluxes obtained by the *IRAS* and the relation established by Kennicutt (1998). To derive the total far-infrared luminosity of the sample galaxies, and hence derive the SFRs, we followed the methodology described in Bogdán et al. (2013a). We concluded that all the sample galaxies had low SFRs relative to their stellar mass, implying that none of the galaxies was a starburst system. The stellar masses and SFRs of the sample galaxies are given in Table 1.

4. RESULTS

4.1. Searching for Hot X-ray Coronae

To identify hot coronae around the sample galaxies, we employed four different methods. First, we searched for diffuse X-ray emission by visually inspecting the background subtracted and vignetting corrected *Chandra* images in a soft (0.3–1 keV), broad (0.3–2 keV), and hard band (1–2 keV). Probing different energy ranges is useful, because it offers the opportunity to detect an ionized gas component with relatively low (<0.3 keV) or higher (>0.3 keV) gas temperatures. While a diffuse X-ray glow is associated with some of the spiral galaxies in our sample, this emission is focused in the innermost regions. However, within these regions several additional X-ray emitting components are present, such as unresolved low-mass and high-mass X-ray binaries, cataclysmic variables, active binaries, young stars, young stellar objects, and diffuse gas associated with star formation (Gilfanov 2004; Revnivtsev et al. 2008; Bogdán & Gilfanov 2011; Mineo et al. 2012). Given the overall difficulty of assessing the importance of each of the above listed components to the diffuse gaseous emission, we must explore the hot coronae beyond the optical radii of the galaxies.

As a second approach, we probed the existence of hot coronae by constructing radial surface brightness profiles for each galaxy in the 0.3–1 keV, 0.3–2 keV, and 1–2 keV bands. To construct the profiles we utilized the background subtracted and vignetting corrected data, and extracted circular annuli centered on the optical centroid of each galaxy. The X-ray profiles were compared with the stellar light distribution inferred from the 2MASS K-band images. Based on these profiles we did not detect an extended X-ray emitting component beyond the optical radii.

Third, to increased the S/N of the data we co-added (i.e., stacked) the individual surface brightness distributions in the three studied energy ranges. In Figure 2, we show the stacked 0.3–2 keV band surface brightness profile of the diffuse X-ray emission, as well as the stacked K-band light distribution.
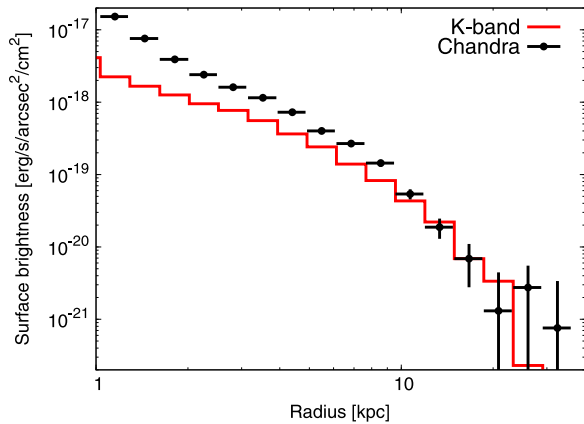
Figure 2. Stacked 0.3–2 keV band X-ray surface brightness profile of the the diffuse emission for the eight galaxies in our sample. To construct the profiles, we used circular annuli centered on the optical centroid of each galaxy. Vignetting correction is applied and all background components are subtracted. The 2MASS K-band surface brightness profile, which traces the stellar light distribution, is over plotted. The K-band light is normalized to match the last X-ray detected bin at ≈17 kpc. Note that the X-ray surface brightness for the last three bins are consistent with 0.

While the X-ray and K-band surface brightness distributions are markedly different, the stacked profile does not reveal a statistically significant diffuse X-ray emitting component beyond ~20 kpc. In agreement with these, the soft and hard band profiles also did not reveal the presence of diffuse X-ray emission beyond the extent of the stellar light.

Finally, we probed the existence of an extended X-ray emitting component in the $(0.05-0.15)r_{200}$ and $(0.15-0.30)r_{200}$ regions in the soft, broad, and hard band *Chandra* data. However, we could not identify statistically significant diffuse X-ray emission in either radial bin. As before, we increased the S/N by stacking the X-ray photons in the three energy ranges. The stacked data also did not reveal a statistically significant signal. Interestingly, we detected a moderately significant (~2σ) X-ray emitting component in the $(0.05-0.15)r_{200}$ region for NGC 266, which possibly originates from its hot gaseous corona. We detected 137 ± 60 net counts in the 0.3–2 keV energy range, where the error range refers to the statistical uncertainties. Given the low S/N, the importance of systematic uncertainties associated with the background subtraction is non-negligible. Specifically, depending on the background subtraction method, the obtained signal exhibits somewhat different (~1.5σ–2.5σ) statistical significance. Despite the low significance detection of the diffuse emission around NGC 266, we note that the observed count rates are broadly consistent with our earlier results presented in Bogdán et al. (2013b)—for further discussion see Section 6.

This evidence, both individually and combined, indicates that statistically significant diffuse X-ray emission is not detected beyond the optical radii ($\gtrsim$20 kpc) of the sample galaxies.

4.2. Constraining the Gas Parameters

In the absence of statistically significant detections of the extended emission beyond the optical radii, we computed 3σ limits on the characteristics of the hot X-ray coronae. To this end, we derived the 3σ upper limits on the X-ray counts in circular annuli with radii of $(0.05-0.15)r_{200}$ and $(0.15-0.30)$ r_{200}, following Bogdán et al. (2013a). We utilized all available

Chandra detectors to maximize the number of detected counts. To convert the counts to physical units, we assumed an optically thin thermal plasma emission (APEC) model with $kT = 0.2$ keV temperature, 0.1 Solar abundance, and Galactic column density. To account for the vignetting effects and the different sensitivity of various detectors, we employed the tailor-made response files for each observation. The upper limits on the X-ray counts were converted to the normalization of the APEC model using:

$$N = \frac{10^{-14}}{4\pi D^2} \int n_e n_H dV,$$

where D is the distance of the galaxy, and n_e and n_H are the electron and hydrogen number densities, respectively. Based on the upper limits on the emission measure ($\int n_e n_H dV$), we computed upper limits on the X-ray luminosity, average gas density, and confined gas mass within the volume that corresponds to the radial ranges of $(0.05-0.15)r_{200}$ and $(0.15-0.30)r_{200}$. Note that in these calculations we assumed that the hot gas has a spherically symmetric distribution and constant gas density within the given bins. Additionally, we derived lower limits on the cooling time, which is computed as $t_{cool} = (3kT)/(n_e \Lambda(T))$, where $\Lambda(T)$ is the cooling function. Finally, we also derived upper limits on the cooling rates of the gas as $\dot{M} = M_{gas}/t_{cool}$, which allowed us to probe whether cooling of the hot gaseous coronae can balance the ongoing star formation in the disk (Section 6).

To place more stringent constraints on the properties of hot coronae, we stacked the X-ray photons along with the corresponding exposure maps for the six most nearby galaxies in our sample: NGC 1097, NGC 2841, NGC 5005, NGC 5170, NGC 5529, and NGC 5746. The stacked data allowed us to compute the average 3σ limits on the gas parameters for spiral galaxies in the stellar mass range of $(0.7-1.4) \times 10^{11} M_\odot$. Thanks to the increased S/N, these limits are more stringent than those obtained for individual galaxies. To derive the 3σ limits on the gas characteristics for the stacked data, we utilized the median distance, virial radius, and column density of the sub-sample, and followed the procedure described for individual galaxies. The limits are given in Table 3.

Although the main focus of this work is to probe the characteristics of hot coronae around lower mass spirals, we extended the present sample using our earlier detections of the coronae around NGC 1961 and NGC 6753 (Bogdán et al. 2013a). Including these galaxies allowed us to confront the Illustris Simulation with observational results in the stellar mass range of $(0.7-4.2) \times 10^{11} M_\odot$.

5. COMPARISON WITH ILLUSTRIS

5.1. The Illustris Simulations

The Illustris Project (http://www.illustris-project.org) comprises a series of cosmological hydrodynamic simulation runs in a $(106.5 \, \text{Mpc})^3$ volume performed with the moving-mesh code AREPO (Springel 2010). The simulations were carried out at a series of resolutions, of which the highest resolution, Illustris-1 (or simply Illustris), has a mass resolution of $m_{DM} = 6.26 \times 10^6 M_\odot$ and $m_{baryon} \simeq 1.26 \times 10^6 M_\odot$ for the dark matter and baryonic components, respectively. At $z = 0$ the co-moving plummer equivalent gravitational softening lengths are 1.4 kpc for the dark matter and 0.7 kpc for baryonic

Table 3
Constraints on the Parameters of the Diffuse Hot Gaseous Coronae

Galaxy	Radial Range r_{200}	$L_{0.5-2\,\text{keV,abs}}$ (erg s^{-1})	L_{bol} (erg s^{-1})	M_{gas} ($M_\odot$)	n_e (cm^{-3})	t_{cool} (Gyr)	$\dot{M}$ ($M_\odot$ yr^{-1})
NGC 266	0.05–0.15	$<1.9 \times 10^{40}$	$<8.9 \times 10^{40}$	$<1.9 \times 10^{10}$	$<8.0 \times 10^{-4}$	>2.9	<6.5
NGC 1097	0.05–0.15	$<1.5 \times 10^{39}$	$<6.1 \times 10^{39}$	$<2.2 \times 10^{9}$	$<5.0 \times 10^{-4}$	>4.6	<0.5
NGC 2841	0.05–0.15	$<2.9 \times 10^{39}$	$<1.1 \times 10^{40}$	$<5.8 \times 10^{9}$	$<3.6 \times 10^{-4}$	>6.4	<0.9
NGC 5005	0.05–0.15	$<2.3 \times 10^{39}$	$<8.7 \times 10^{39}$	$<3.3 \times 10^{9}$	$<4.9 \times 10^{-4}$	>4.7	<0.7
NGC 5170	0.05–0.15	$<3.0 \times 10^{39}$	$<1.6 \times 10^{40}$	$<4.3 \times 10^{9}$	$<6.6 \times 10^{-4}$	>3.5	<1.2
NGC 5529	0.05–0.15	$<4.7 \times 10^{39}$	$<1.8 \times 10^{40}$	$<5.8 \times 10^{9}$	$<5.6 \times 10^{-4}$	>4.1	<1.4
NGC 5746	0.05–0.15	$<3.0 \times 10^{39}$	$<1.3 \times 10^{40}$	$<5.9 \times 10^{9}$	$<4.0 \times 10^{-5}$	>5.7	<1.0
ESO 445-081	0.05–0.15	$<2.9 \times 10^{40}$	$<1.4 \times 10^{41}$	$<4.1 \times 10^{10}$	$<6.0 \times 10^{-4}$	>3.8	<10.9
STACK[a]	0.05–0.15	$<2.0 \times 10^{39}$	$<7.3 \times 10^{39}$	$<3.2 \times 10^{9}$	$<3.8 \times 10^{-4}$	>6.0	<0.5
NGC 266	0.15–0.30	$<4.0 \times 10^{40}$	$<1.9 \times 10^{41}$	$<7.3 \times 10^{10}$	$<4.4 \times 10^{-4}$	>5.3	<13.8
NGC 1097	0.15–0.30	$<2.9 \times 10^{39}$	$<1.2 \times 10^{40}$	$<8.4 \times 10^{9}$	$<2.6 \times 10^{-4}$	>8.9	<0.9
NGC 2841	0.15–0.30	$<1.7 \times 10^{39}$	$<6.6 \times 10^{39}$	$<1.2 \times 10^{10}$	$<1.0 \times 10^{-4}$	>22.4	<0.5
NGC 5005	0.15–0.30	$<5.0 \times 10^{39}$	$<1.9 \times 10^{40}$	$<1.3 \times 10^{10}$	$<2.7 \times 10^{-4}$	>8.6	<1.5
NGC 5170	0.15–0.30	$<4.3 \times 10^{39}$	$<2.2 \times 10^{40}$	$<1.4 \times 10^{10}$	$<3.0 \times 10^{-4}$	>7.8	<1.8
NGC 5529	0.15–0.30	$<8.0 \times 10^{39}$	$<3.0 \times 10^{40}$	$<2.1 \times 10^{10}$	$<2.7 \times 10^{-4}$	>8.4	<2.4
NGC 5746	0.15–0.30	$<2.1 \times 10^{39}$	$<9.0 \times 10^{39}$	$<1.3 \times 10^{10}$	$<1.2 \times 10^{-4}$	>18.3	<0.7
ESO 445-081	0.15–0.30	$<6.4 \times 10^{40}$	$<3.1 \times 10^{41}$	$<1.7 \times 10^{11}$	$<3.3 \times 10^{-4}$	>6.8	<24.4
STACK[a]	0.15–0.30	$<2.7 \times 10^{39}$	$<9.8 \times 10^{39}$	$<1.0 \times 10^{10}$	$<1.6 \times 10^{-4}$	>14.4	<0.7

[a] Based on the stacked data of a sub-sample of six galaxies: NGC 1097, NGC 2841, NGC 5005, NGC 5170, NGC 5529, and NGC 5746.

collisionless particles, whereas for gas it is adaptively set by the cell size, but cannot be lower than 0.7 kpc. In this paper, we relied on the results of the Illustris run. The Illustris Simulation discussed here adopts cosmological parameters consistent with the *WMAP*-9 measurements (Hinshaw et al. 2013).

Illustris incorporates the crucial physical processes that are indispensable to describe galaxy formation and evolution (Vogelsberger et al. 2014a, 2014b; Genel et al. 2014). Specifically, it includes primordial and metal line cooling, describes the stellar evolution and the corresponding feedback processes, traces the chemical enrichment processes by modeling nine elements, seeds supermassive black holes and follows their evolution through accretion and mergers, and models the energetic quasar-mode and radio-mode feedback of supermassive black holes. Details of the incorporated physics modules were discussed in previous works (Vogelsberger et al. 2013; Torrey et al. 2014). A major consequence of the implemented stellar and AGN feedback is that the Illustris simulation can produce a stellar mass—halo mass relation, which is in good agreement with that observed from abundance matching studies. Additionally, Illustris can successfully reproduce the observed cosmic star-formation density, and can result in a realistic galaxy population. Overall, Illustris offers an ideal framework to confront the observed and simulated properties of hot X-ray coronae.

Following our observational approach, we derive the characteristics of the hot gas in Illustris in two radial ranges. We utilize the $0.05r_{200} < r < 0.15r_{200}$ and $0.15r_{200} < r < 0.30r_{200}$ regions for the inner and outer regions, respectively. Since we aim to study the hot gas, we only included gas particles that have a temperature of at least 1.16×10^6 K. To derive the X-ray luminosity and other properties of the gas, we follow the procedure described in Navarro et al. (1995).

5.2. X-ray Luminosities and Gas Masses

Since the X-ray luminosity and gas mass of the hot coronae have been widely used to test galaxy formation models, we first

confronted these quantities with those predicted by Illustris. To facilitate the comparison with previous and subsequent works, we performed the comparison in the $(0.05-0.15)r_{200}$ and $(0.15-0.30)r_{200}$ radial ranges.

When investigating the full sample, Illustris predicts large scatter in the X-ray luminosity and gas mass at every stellar mass (Figures 3 and 4). Moreover, the median X-ray luminosities and gas masses show an increasing trend in the stellar mass range of $(0.2-1) \times 10^{11}\,M_\odot$, whereas in $M_\star = (1-6) \times 10^{11}\,M_\odot$ these values decline or remain broadly constant. The reason for the relatively low luminosities and gas masses at $M_\star \gtrsim 10^{11}\,M_\odot$ is that radio-mode AGN feedback becomes dominant above these masses. As discussed in Genel et al. (2014), the radio-mode feedback was tuned in such a way that it can effectively suppress the star formation in massive halos. This, in turn, blows out a significant fraction of the gas from these massive halos thereby resulting in less massive and less luminous X-ray coronae. For galaxies with less massive black holes, such as those residing in low-mass ellipticals or spirals, the radio-mode feedback is not dominant due to the weaker outbursts. This suggests that spiral galaxies in Illustris host more luminous X-ray coronae than ellipticals. To directly probe this possibility, we compared the median simulated X-ray luminosities for the textbook spiral and elliptical galaxies in the stellar mass range of $(0.7-1.4) \times 10^{11}\,M_\odot$. Because the median stellar and total halo mass of both sub-samples are identical, the different X-ray luminosities cannot be attributed to differences in the depth of the gravitational potential well. We found that within the $(0.05-0.15)r_{200}$ region the median luminosity for textbook spirals ($L_{\text{bol}} = 4.8 \times 10^{39}$ erg s^{-1}) exceeds the median luminosity of textbook ellipticals ($L_{\text{bol}} = 1.1 \times 10^{38}$ erg s^{-1}) by factor of ~44. This conclusion contradicts observational results. Indeed, due to their more luminous nature, gaseous coronae around massive ellipticals are routinely observed (Forman et al. 1985; O'Sullivan et al. 2001; Mathews & Brighenti 2003; Bogdán &
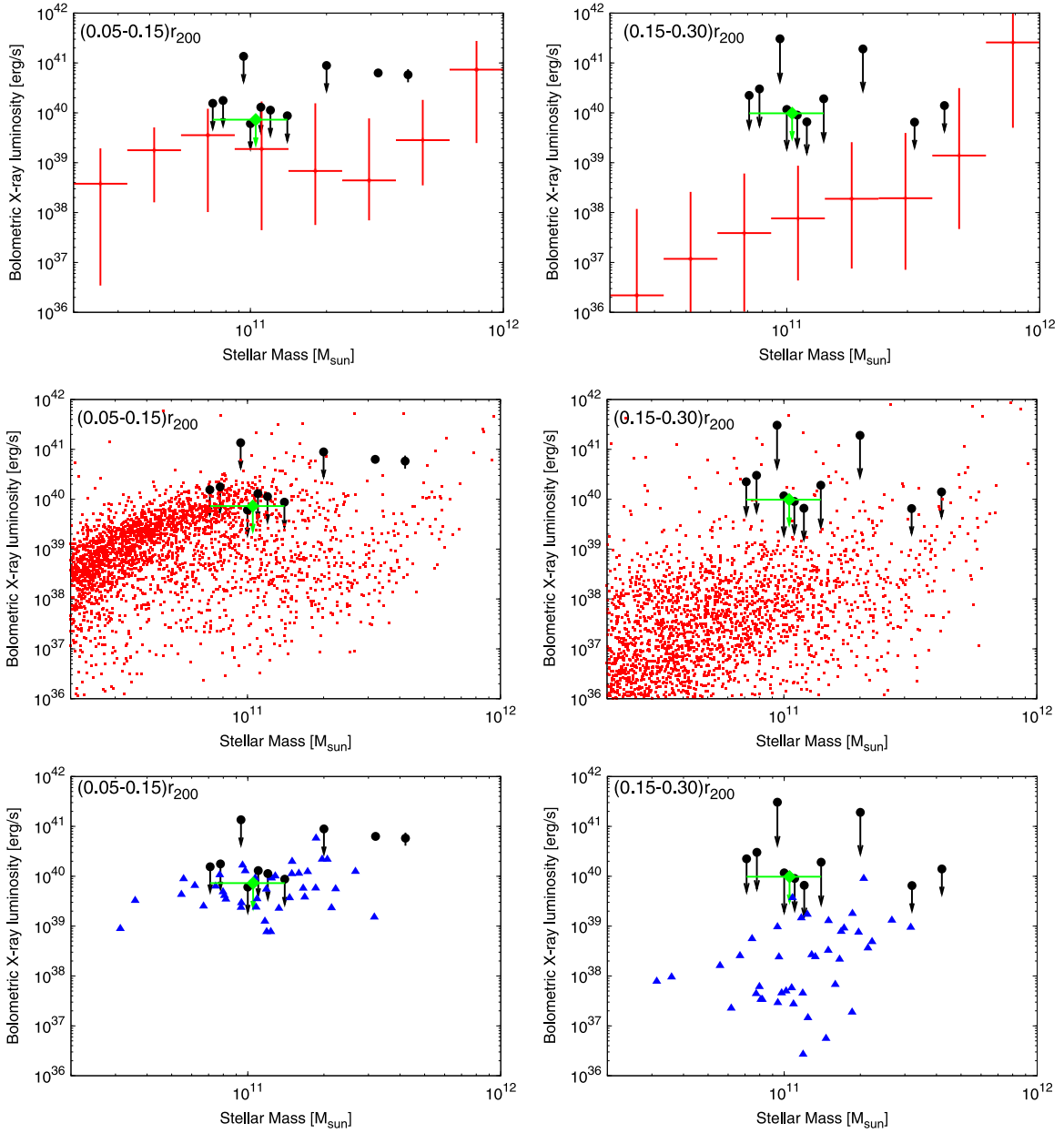
Figure 3. Bolometric X-ray luminosity in the $(0.05–0.15)r_{200}$ (left panels) and $(0.15–0.30)r_{200}$ (right panels) region as a function of the stellar mass. The upper panels show the 10–90 percentile range of the predicted X-ray luminosities in the Illustris Simulation for all simulated galaxies within the stellar mass range of $(2 \times 10^{10}–10^{12} \, M_\odot)$. For each stellar mass bin the median X-ray luminosity is marked with the horizontal bars. The small points in the middle panels depict the individual predicted X-ray luminosities of all simulated galaxies. In the lower panel, triangles show the simulated X-ray luminosity of 42 massive spiral galaxies from Illustris. The large filled circles show the observed X-ray luminosities for NGC 1961 and NGC 6753 (Bogdán et al. 2013a), along with the 3σ upper limits presented in this work. The large filled diamonds with horizontal bars represent the 3σ upper limits on the X-ray luminosity derived from the stacked data of a sub-sample of the six most nearby galaxies. The uncertainty in the observed X-ray luminosity for NGC 6753 is consistent with the size of the symbol (Bogdán et al. 2013a). Note that there is a large scatter in the predicted X-ray luminosity at stellar masses $>10^{11} \, M_\odot$. The scatter and the nearly constant predicted X-ray luminosity for galaxies with stellar mass above $\sim 10^{11} \, M_\odot$ is the consequence of powerful radio-mode AGN feedback, which ejects a significant amount of hot gas from the halos.

Gilfanov 2011), as opposed to the significantly fainter and less explored coronae around spirals.

In the $(0.05–0.15)r_{200}$ region, the observed 3σ upper limits on the X-ray luminosities and gas masses are at the upper end of the simulated values when considering the full Illustris galaxy population. When focusing on the 42 simulated textbook spirals, we conclude that the observed 3σ limits are at the upper end of the model predictions. Specifically, the observed limits on the luminosities and gas masses for the stacked sub-sample exceed the median

simulated values for the textbook spirals. In the $(0.15–0.30)$ r_{200} range the median predicted luminosities and gas masses fall significantly short of the predicted upper limits. Based on these, we conclude that the Illustris predictions do not contradict the observational results for spiral galaxies in the stellar mass range of $(0.7–2.0) \times 10^{11} \, M_\odot$. However, the predicted luminosities and gas masses are significantly lower than those observed for NGC 1961 and NGC 6753, which can be attributed to the overly powerful radio-mode feedback present in Illustris.
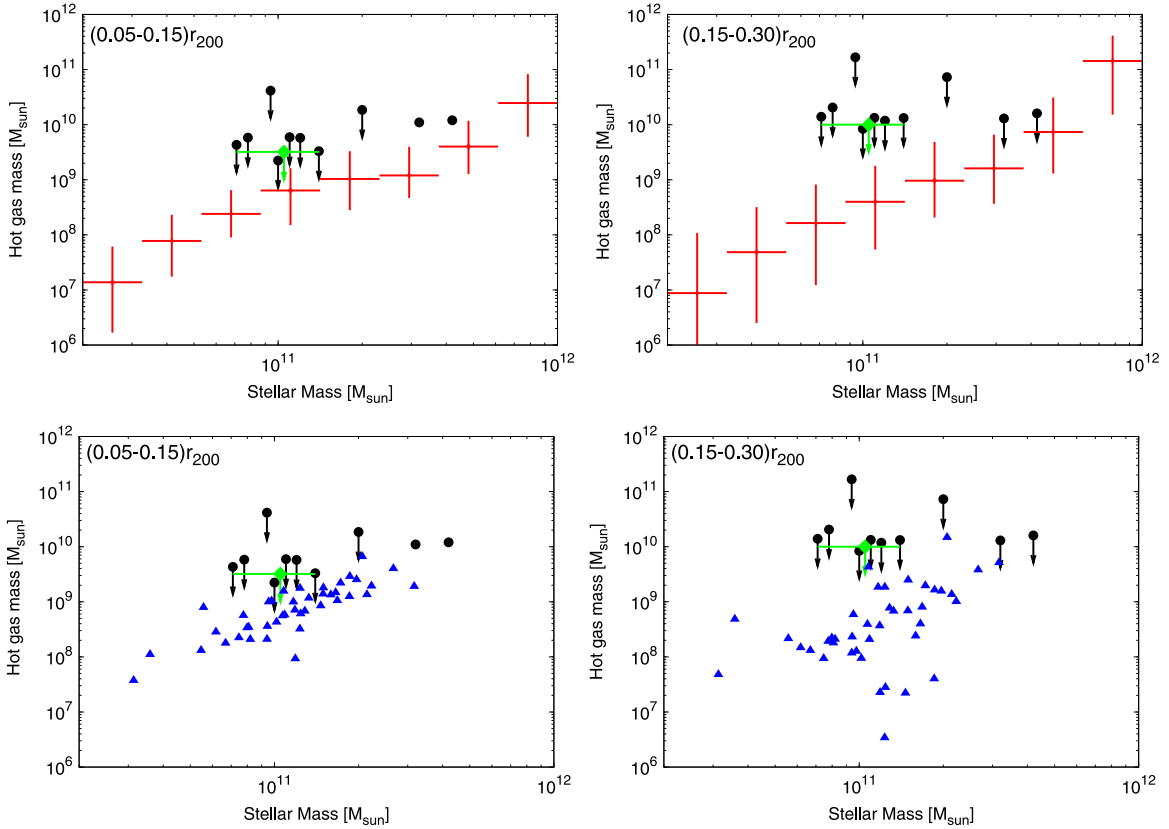
Figure 4. Hot X-ray gas mass confined within the $(0.05–0.15)r_{200}$ (left panel) and $(0.15–0.30)r_{200}$ (right panel) regions as the function of the stellar mass. In the upper panels, the 10–90 percentile range of the simulated gas masses is shown with vertical bars, while the horizontal bars show the median gas mass at the given stellar mass range. In the lower panels, we depict the simulated gas masses of the 42 textbook spiral galaxies. Note that only those gas particles with a temperature of at least 0.1 keV were included in the simulations. Large filled circles represent the observed 3σ upper limits and the observed hot gas masses for NGC 1961 and NGC 6753 (Bogdán et al. 2013a). The uncertainty in the observed gas mass for NGC 1961 and NGC 6753 is consistent with the size of the symbols (Bogdán et al. 2013a). The large filled diamonds with horizontal bars represent the 3σ upper limits on the X-ray luminosity derived from the stacked data of a sub-sample of the six most nearby galaxies.

5.3. Gas Temperature and Abundance

Although the non-detections of hot coronae do not allow us to constrain the gas temperatures and metal abundances, we utilize our previous measurements for NGC 1961 and NGC 6753 (Bogdán et al. 2013a). To this end, we confront the predicted luminosity-weighted temperatures and abundances with the observed values within the $(0.05–0.15)r_{200}$ region. Because the 42 simulated textbook spirals are less massive than the observed galaxies, we focus on the entire Illustris population.

Whereas galaxies with $M_\star \lesssim 10^{11} M_\odot$ are expected to have 0.1–0.2 keV gas temperatures, the predicted temperatures show a rapid increase for more massive galaxies. The observed gas temperatures for NGC 1961 and NGC 6753 are $kT \sim$ 0.6–0.7 keV, which agrees with those predicted by the Illustris simulation.

The right panel of Figure 5 reveals that Illustris predicts $\sim$0.01–0.05 Solar median metal abundances for all galaxies in the studied stellar mass range. While the observed values exceed the simulated ones by a factor of a few, we do not consider this difference to be robust due to the notable systematic uncertainties associated with the abundance measurements (Bogdán et al. 2013a). To further constrain the major metal enrichment processes, deep X-ray observations are required, which can provide the sensitivity to account for the systematic uncertainties in the abundance measurements,

thereby constraining the metal enrichment processes in greater detail.

5.4. Electron Density Profiles

To further probe Illustris, we confront the predicted electron density profiles with those observed for NGC 1961 and NGC 6753 (Bogdán et al. 2013a). The right panel of Figure 6 depicts 61 Illustris galaxies with stellar and virial masses in the range of $(3.0–4.5) \times 10^{11} M_\odot$ and $(0.5–4.2) \times 10^{13} M_\odot$, respectively. These values are in agreement with those of NGC 1961 and NGC 6753. In the right panel of Figure 6, we compare the observed density profiles with the predicted density profiles of the 42 simulated textbook spiral galaxies. These galaxies, on average, are less massive than NGC 1961 and NGC 6753.

When comparing the density profiles of the 61 massive simulated galaxies with those of NGC 1961 and NGC 6753, we conclude that the normalization and shapes of the profiles are broadly similar. However, the agreement is not perfect because the average normalization of the simulated profiles is somewhat lower than that observed for NGC 1961 and NGC 6753, and beyond $\sim$0.1r_{200} the slope of the simulated profiles is steeper than the observed ones. As a caveat, we emphasize that the density profiles for NGC 1961 and NGC 6753 are extrapolated beyond $\sim$0.15r_{200}, and hence carry significant uncertainties. Therefore, it is not clear how much weight should be given to
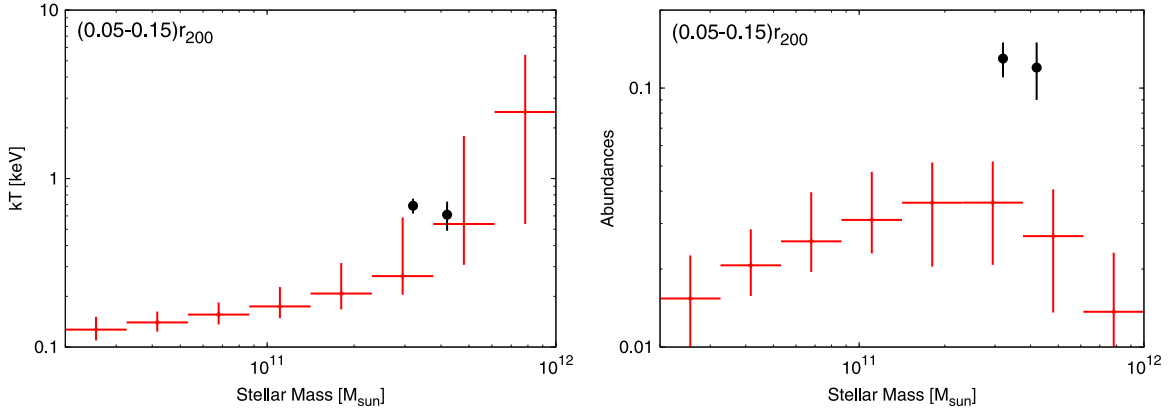
Figure 5. The left and right panels show the temperature and metal abundances of the hot gas within the $(0.05–0.15)r_{200}$ region as a function of the stellar mass, respectively. Both the gas temperature and the abundance refer to luminosity-weighted quantities. The vertical bars show the 10–90 percentile range, and the horizontal bars show the median values for each stellar mass bin. The observed values for NGC 1961 and NGC 6753 are shown for comparison. Note that to date only these two galaxies offer a measurement of the gas temperature and abundance beyond their optical body.
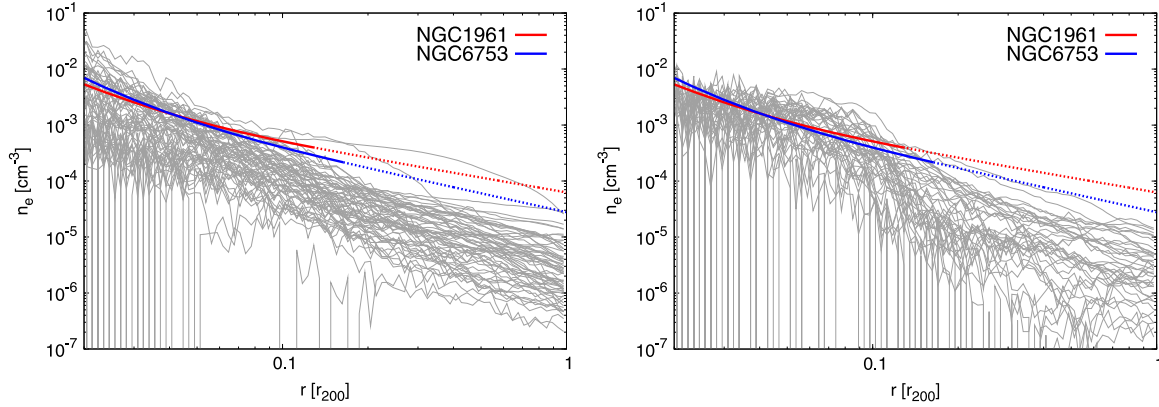
Figure 6. Electron density profiles as a function of radius. In the left panel, the light gray lines show the simulated profiles for the 61 galaxies in the Illustris simulation, whose stellar masses are in the range of $(3.0–4.5) \times 10^{11} M_{\odot}$. In the right panel, the light gray lines represent the 42 massive spiral galaxies. Note that the stellar mass of these textbook spirals is in the range of $(0.3–3.2) \times 10^{11} M_{\odot}$, and hence remains below the stellar masses of NGC 1961 or NGC 6753. The thick red and blue lines represent the observed density profiles for NGC 1961 and NGC 6753, respectively. The short dashed red and blue lines show the extrapolation of the density profiles based on the best-fit modified β-models (Bogdán et al. 2013b). The regions $\lesssim 0.02r_{200}$ are not plotted because they are not well resolved close to the gravitational softening scale, and are not sampled by a large number of particles, which results in larger uncertainties. The radius is measured in units of r_{200}.

the fact that the observed and simulated profiles exhibit somewhat different slopes at large radii.

A similar picture is obtained when we probe the electron density profiles of the 42 simulated textbook spirals. Interestingly, these profiles have similar normalization to those of NGC 1961 and NGC 6753, despite the fact that the Illustris galaxies have lower average stellar mass. Beyond $\sim 0.1r_{200}$ the simulated profiles decline more steeply, which may be a combined effect of the lower gas mass in these halos and the powerful radio-mode AGN feedback, which ejects the hot gas to larger radii and/or removes it from the dark matter halos of galaxies.

6. DISCUSSION

Since we are studying spiral galaxies with SFRs in the $\sim 1–6\ M_{\odot}\ \mathrm{yr}^{-1}$ range, it is important to determine whether these galaxies could be prone to starburst-driven winds at the present epoch. Theoretical calculations indicate, and observational results confirm, that in galaxies with the area-specific supernova rate of $>40\ \mathrm{SN\ Myr^{-1}\ kpc^{-2}}$ the detection of extraplanar emission is expected (Strickland et al. 2004). Note

that the surface area is defined as $A = D_{25}^2$, where D_{25} is the diameter of the isophote having the surface brightness of 25 mag arcsec^{-2}. To derive the specific supernova rates, we compute the supernova rate as $R_{\mathrm{SN}} = 0.2L_{\mathrm{FIR}}/10^{11}\ L_{\odot}$, where L_{FIR} is the total far-infrared luminosity (Heckman et al. 1990), and use the D_{25} radii given in Table 1. We find that the supernova rates are in the range of $0.005–0.068\ \mathrm{yr}^{-1}$, and the observed area-specific supernova rates are in the range of $\sim 2–36\ \mathrm{Myr^{-1}\ kpc^{-2}}$ for all galaxies but NGC 5005 and ESO 445-081. Thus we do not expect extraplanar gaseous emission driven by the energy input of supernovae for the six galaxies in our sample. While the specific supernova rates for NGC 5005 and ESO 445-081 exceed the critical rate, they remain below the values obtained for well-known starburst galaxies, such as M82 (Strickland et al. 2004). Therefore, while we may expect an outflow in NGC 5005 and ESO 445-081, these are likely less prominent than those in starburst galaxies, hinting that the hot gaseous coronae are not dominated by hot gas originating from starburst-driven winds. As a caveat, we mention that at earlier epochs these galaxies likely underwent more active evolutionary phases characterized

by gas-rich (minor) mergers, which may have brought a significant supply of cold gas, thereby triggering starburst-driven winds. These starburst-driven winds at high redshifts presumably played a role in lifting a certain amount of hot gas to larger radii, as well as enriching the hot gas originating from infall.

From the derived upper limits on the gas mass and the lower limits on the cooling time, we obtain upper limits on the cooling rates as $\dot{M} = M_{gas}/t_{cool}$. Using this estimate we probe whether the cooling of the hot corona can balance the ongoing star formation in the disk. We find that the combined upper limits on the cooling rate in $(0.05–0.30)r_{200}$ exceed or are comparable to the observed SFRs for all galaxies in our sample. Additionally, the cooling of the hot gas in the innermost regions $(<0.05r_{200})$ may also contribute, because this gas is expected to be denser, and hence have a shorter cooling time. This implies that cooling of the gas in the corona may be able to provide the cold gas required for the ongoing star formation. We note that this result is in contrast with that observed for NGC 1961 and NGC 6753, which host significantly hotter gas with cooling times that exceed the Hubble-time.

Although the *Chandra* observations of NGC 266 did not reveal a statistically significant detection of a hot gaseous corona, this result is not in conflict with our earlier detection based on *ROSAT* observations. Specifically, within the $(0.05–0.15)r_{200}$ region, the observed *ROSAT* count rate was $\sim 3.4 \times 10^{-3}$ s^{-1} (Bogdán et al. 2013b). By contrast, the count rate detected by *Chandra* is $\sim 1.1 \times 10^{-3}$ s^{-1}. Taking into account the effective area of the *ROSAT* PSPC and the *Chandra* ACIS-I detectors, we conclude that the factor of ~ 3 difference in the count rates may be due to the low temperature of the hot gas. Specifically, our observational results are consistent with a picture in which the hot gas corona surrounding NGC 266 has a temperature of $kT \sim 0.15$ keV. Thus, the non-detection of the hot corona around NGC 266 in the deep *Chandra* observations is likely due to the combined effects of the low ACIS-I effective area below the 0.5 keV energy and the low gas temperature.

Because—in the absence of statistically significant detections—we assumed a spectral model to derive upper and lower limits on various parameters of the hot gas in this work, we briefly overview the uncertainties that may be associated with the chosen spectral model. A notable source of uncertainty arises from the unknown gas temperatures. For example, if the gas temperature is factor of two lower or higher than the assumed 0.2 keV, that would imply a factor of about two higher or lower counts-to-flux conversion for the ACIS-S detector, and factor of about three difference for galaxies observed with the ACIS-I detector. Additionally, the unknown metal abundances may also significantly influence the conversion. For example, if the metal abundance are five times higher or lower than the assumed 0.1 Solar abundance, that would yield a factor of ~ 2 increase or decrease in the gas densities and gas masses.

In the present study we could not identify a so-far unexplored hot corona, so the number of galaxies with detected coronae remains four: NGC 1961, UGC 12591, NGC 6753, and NGC 266 (Anderson & Bregman 2011; Dai et al. 2012; Bogdán et al. 2013a, 2013b). There are two major reasons for the difficulty in identifying hot coronae around spiral galaxies with present-day telescopes. First, the detectable X-ray surface brightness of the coronae is low, due to their relatively faint but extended nature. As a result, the observed S/N, particularly for lower mass galaxies, does not allow coronae to be detected unambiguously. Second, as pointed out by Illustris, the gas temperatures drop rapidly for galaxies with $M_\star \lesssim 3 \times 10^{11}\,M_\odot$. However, *Chandra* and *XMM-Newton* have relatively low effective areas at energies below ~ 0.5 keV, and hence are not sufficiently sensitive to thermal emission with ~ 0.1–0.2 keV. Additionally, for such low temperatures, the hot gaseous emission is prone to absorption, which in turn can drastically reduce the observed X-ray flux. The combination of these effects makes it difficult to detect hot coronae around lower mass spiral galaxies, particularly at radii exceeding $\sim 0.15r_{200}$.

7. CONCLUSIONS

In this paper, we studied the hot gaseous coronae around eight normal spiral galaxies, whose stellar mass is in the range of $(0.7–2.0) \times 10^{11}\,M_\odot$, using *Chandra* X-ray observations. To confront the observations with galaxy formation models, we utilized the hydrodynamical cosmological simulation, Illustris. Our results are summarized below.

1. We did not detect a statistically significant hot corona around any of our sample galaxies in the $(0.05–0.15)r_{200}$ or $(0.15–0.30)r_{200}$ radial ranges. However, for NGC 266 we identified the presence of a moderately significant $(\sim 2\sigma)$ extended X-ray emitting component in the $(0.05–0.15)r_{200}$ region, which may originate from hot ionized gas. This result is in agreement with our earlier detection based on *ROSAT* data (Bogdán et al. 2013b).

2. In the absence of statistically significant detections, we derived 3σ limits on the X-ray luminosity, confined gas mass, electron densities, and cooling times. To derive these limits, we assumed that the hot gas is spherically symmetric, has a temperature of $kT = 0.2$ keV, and metal abundances of 0.1 Solar.

3. The derived upper and lower limits, complemented with the gas parameters measured for NGC 1961 and NGC 6753, were compared to the results of the Illustris Simulation. We concluded that the observed 3σ upper limits on the X-ray luminosity and hot gas mass exceed or were at the upper end of the model predictions. For NGC 1961 and NGC 6753, we found that the gas temperatures, metal abundances, and electron density profiles broadly agreed with the model predictions. These results imply that the observed properties of X-ray coronae around spirals are broadly consistent with those predicted by Illustris. However, for galaxies with massive black holes (mostly giant ellipticals), Illustris predicts overly powerful radio-mode feedback, which in turn results in under-luminous X-ray coronae in these systems.

REFERENCES

Anderson, M. E., & Bregman, J. N. 2011, ApJ, 737, 22
Bell, E. F., McIntosh, D. H., Katz, N., & Weinberg, M. D. 2003, ApJS, 149, 289
Benson, A. J., Bower, R. G., Frenk, C. S., & White, S. D. M. 2000, MNRAS, 314, 557
Bogdán, Á, & Gilfanov, M. 2008, MNRAS, 388, 56
Bogdán, Á, & Gilfanov, M. 2011, MNRAS, 418, 1901
Bogdán, Á, Forman, W. R., Vogelsberger, M., et al. 2013a, ApJ, 772, 97
Bogdán, Á, Forman, W. R., Kraft, R. P., & Jones, C. 2013b, ApJ, 772, 98
Crain, R. A., McCarthy, I. G., Frenk, C. S., Theuns, T., & Schaye, J. 2010, MNRAS, 407, 1403
Dai, X., Anderson, M. E., Bregman, J. N., & Miller, J. M. 2012, ApJ, 755, 107
Forman, W., Jones, C., & Tucker, W. 1985, ApJ, 293, 102
Genel, S., Vogelsberger, M., Springel, V., et al. 2014, arXiv:1405.3749
Gilfanov, M. 2004, MNRAS, 349, 146
Grevesse, N., & Sauval, A. J. 1998, SSRv, 85, 161
Heckman, T. M., Armus, L., & Miley, G. K. 1990, ApJS, 74, 833
Hinshaw, G., Larson, D., Komatsu, E., et al. 2013, ApJS, 208, 19
Jarrett, T. H., Chester, T., Cutri, R., Schneider, S. E, & Huchra, J. P. 2003, AJ, 125, 525
Kalberla, P. M. W., Burton, W. B., Hartmann, D., et al. 2005, A&A, 440, 775
Kennicutt, R. C., Jr. 1998, ARA&A, 36, 189
Li, J.-T., Crain, R. A., & Wang, Q. D. 2014, MNRAS, 440, 859
Li, Z., Jones, C., & Forman, W. R. 2011, ApJ, 730, 84
Li, Z., Wang, Q. D., Irwin, J. A., & Chaves, T. 2006, MNRAS, 371, 147
Li, J.-T., & Wang, Q. D. 2013, MNRAS, 428, 2085
Marinacci, F., Pakmor, R., Springel, V., & Simpson, C. M. 2014, MNRAS, 442, 3745
Mathews, W. G., & Brighenti, F. 2003, ARA&A, 41, 191
Mineo, S., Gilfanov, M., & Sunyaev, R. 2012, MNRAS, 419, 2095
Navarro, J. F., Frenk, C. S., & White, S. D. M. 1995, MNRAS, 275, 720
O'Sullivan, E., Forbes, D. A., & Ponman, T. J. 2001, MNRAS, 328, 461
Rasmussen, J., Sommer-Larsen, J., Pedersen, K., et al. 2009, ApJ, 697, 79
Revnivtsev, M., Churazov, E., Sazonov, S., Forman, W., & Jones, C. 2008, A&A, 490, 37
Snowden, S. L., Egger, R., Freyberg, M. J., et al. 1997, ApJ, 485, 125
Springel, V. 2010, MNRAS, 401, 791
Strickland, D. K., Heckman, T. M., Colbert, E. J. M., Hoopes, C. G., & Weaver, K. A. 2004, ApJ, 606, 829
Toft, S., Rasmussen, J., Sommer-Larsen, J., & Pedersen, K. 2002, MNRAS, 335, 799
Torrey, P., Vogelsberger, M., Genel, S., et al. 2014, MNRAS, 438, 1985
Tully, R. B., Rizzi, L., Shaya, Edward, J., et al. 2009, AJ, 138, 323
Vogelsberger, M., Sijacki, D., Keres, D., Springel, V., & Hernquist, L. 2012, MNRAS, 425, 3024
Vogelsberger, M., Genel, S., Sijacki, D., et al. 2013, MNRAS, 436, 3031
Vogelsberger, M., Genel, S., Springel, V., et al. 2014a, Natur, 509, 177
Vogelsberger, M., Genel, S., & Springel, V. 2014b, MNRAS, 444, 1518
White, S. D. M., & Frenk, C. S. 1991, ApJ, 379, 52
White, S. D. M., & Rees, M. J. 1978, MNRAS, 183, 341